Aerospace Science and Technology 30 (2013) 83–93

Contents lists available at ScienceDirect

Aerospace Science and Technology

www.elsevier.com/locate/aescte

Experimental analysis of the pressure–velocity correlations of external unsteady flow over rocket launchers

S. Marié [a,*], Ph. Druault [b,c], H. Lambaré [d], F. Schrijer [e]

[a] Conservatoire National des Arts et Métiers, Laboratoire DynFluid, 151, boulevard de l'Hôpital, 75013 Paris, France
[b] University Pierre and Marie Curie – Paris 6, UMR 7190, Institut Jean Le Rond d'Alembert, case 162, 4, Place Jussieu, 75252 Paris Cedex 05, France
[c] CNRS, UMR 7190, Institut Jean Le Rond d'Alembert, 75252 Paris Cedex 05, France
[d] CNES, Direction des Lanceurs, 52 rue Jacques Hillairet, 75612 Paris cedex, France
[e] Delft University of Technology, Fac. of Aerospace Engineering, Netherlands

ARTICLE INFO

Article history:
Received 15 June 2012
Received in revised form 25 April 2013
Accepted 16 July 2013
Available online 28 August 2013

Keywords:
Pressure–velocity correlation
Launcher after-body
Proper orthogonal decomposition
Unsteady reattached flow

ABSTRACT

Based on simultaneous wall pressure and velocity measurements, the aerodynamic load of a launcher body model is investigated. Two different configurations are considered in order to study the influence of geometrical artifacts on the after-body flow and consequently on the aerodynamic load. After a brief presentation of the experimental setup used to get the unsteady wall pressure and external velocity field, a global analysis of the integrated pressure along the nozzle is presented for both configurations. It is shown that the unsteady load induced on a configuration with attachment device involves characteristic frequencies which fits the mechanical response of the structure whereas no particular behavior is observed on the configuration without attachment device. Then, a Proper Orthogonal Decomposition (POD) is successively performed from the wall pressure field and from the external velocity field highlighting the relationship between the most energetic structures of the flow and the involved phenomenon. Finally, a pressure–velocity correlation of the POD modes is presented and the most energetic structures of the velocity field are linked to the unsteady load observed on the nozzle. It is then confirmed the structural influence of the attachment device and its contribution to the unsteady loads acting on the nozzle.

1. Introduction

In order to increase the capabilities of rocket launchers, it is necessary to develop higher performance propulsion systems. A way of achieving this is by using larger expansion area ratio nozzles. However during the operation, and in particular during the transonic phase (Mach number around 0.8), high amplitude excitations are observed on the launcher nozzle. In fact, the external and unsteady base flow has been recognized as an important issue since the first launch of the Ariane 5 launcher. It is now clear that the rear-part of such a rocket is the home of complex phenomena potentially involving loads on the main nozzle. From a mechanical point of view, the nozzle is characterized by two main structural modes associated with two identified frequencies. During the transonic flight, frequencies associated with the external aerodynamic loads are unfortunately the same as the mechanical ones which leads to undesirable nozzle vibrations [3,8]. This is then essential to properly investigate the aerodynamic flow responsible for such a phenomenon.

Dynamic loads on the nozzle are caused by fluctuating pressure induced by a massively detached and turbulent flow dominated by two main phenomena: (1) a peaked one occurring around the Strouhal number of $St = 0.2$ associated with a frequency of 10 Hz at Mach number, $M = 0.8$, and (2) a broad-band excitation around the Strouhal number of 0.5. Such well known phenomena have been previously investigated experimentally [3,8,9] as well as numerically [2,24] on axisymmetric step flow configuration. In this work, based on experimental investigations performed on an Ariane 5 model, we focus on the external part of the flow field and its associated side-load contribution. Previous experimental studies have been already performed to analyze the aerodynamic flow field inducing the external load effect on the launcher. Garçon and Drevet [8] have experimentally investigated the unsteady aerodynamic loads applied on a 1:60 scaled model of the main Ariane 5 launcher nozzle. They then emphasized the great difficulty in measuring such aerodynamic loads. In their work, the balance measurement technique was tested and recommendation about the calibration and inertia load correction was investigated. Deprés et al. [3] have experimentally investigated the transonic buffeting phenomenon. They showed that the ratio between the nozzle length and the body diameter has a great influence on the unsteady developing flow and then on the resulting side-load effect.

* Corresponding author.
E-mail address: simon.marie@cnam.fr (S. Marié).

1270-9638/$ – see front matter
http://dx.doi.org/10.1016/j.ast.2013.07.006

Nomenclature

PIV	Particle Image Velocimetry
POD	Proper Orthogonal Decomposition
$[C^u_{F^z_m}]^l_k$	correlation between the load $\{F^z_m\}^k_1$ and streamwise velocity $\{U\}^l_1$
D	central body diameter (reference length)
$\mathbf{F}_m$	mth Fourier mode of the load computed with integrated wall pressure
F^z_m	mth Fourier mode of the load projected onto z-axis
$\{F^z_m\}^l_k$	mth Fourier mode of the load computed with pressure POD modes from k to l
G^z_m	Power Spectral Density (PSD) of the mth Fourier mode of the projected load
M_0	Free-stream Mach number
St	Strouhal number (fD/U_0)
$\{U\}^l_k$	Streamwise velocity field projected onto POD modes from k to l
U_0	Free-stream velocity
α	incidence angle
β	yaw angle
θ	azimuthal coordinate: $(\widehat{Oy}, \widehat{Oz})$
θ_0	azimuthal position of the first sensor on a ring
$\Delta\theta$	azimuthal space between two sensors on a ring

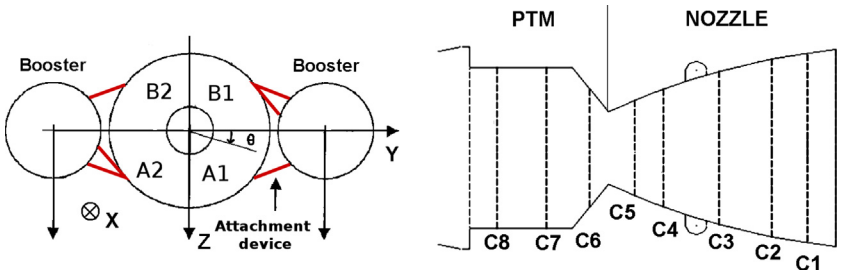

Fig. 1. Left-hand side: Rear view of the geometry and axes of the model. Parts A1 to B2 are identified here for further investigating side-load effects. Right-hand side: Position of 8 rings along with unsteady pressure transducers are located (see Table 2). (For interpretation of the references to color in this figure, the reader is referred to the web version of this article.)

Wong et al. [25] analyzed wall pressure measurements obtained from more than 40 pressure transducers distributed uniformly over the Ariane 5 after-body. These measurements have been conducted with different free-stream Mach numbers ranging from 0.4 to 0.9. Based on the cross-correlation and coherence function analysis of resulted wall pressure field, great indications (like resonant frequencies) have been provided about the forces acting on the structure. They stated that further experiments have to be performed to confirm these first results. Based on another experimental database using pressure transducers located on the nozzle of a launcher, Geurts [9] highlighted a high level of transverse load on the nozzle which can be attributed to a particular flow structure organization due to the coupling of vortices generated near the boosters and the recirculation zone downstream the central body. Finally, for such a flow configuration, very few data (pressure and velocity) are available in the literature allowing (i) the investigation of the nozzle geometrical effect onto side loads and (ii) the investigation of the coupling between wall pressure load and external aerodynamic flow field. For such a purpose, some measurement methods coupled to post-processing mathematical tools need to be developed to better understand the involved flow phenomenon. Based on simultaneous wall pressure and velocity measurements, the goal of this work is to enhance the knowledge of aerodynamic load on the nozzle and especially the effect of the geometry. A particular attention will be given to the rear attachment device which connects the boosters to the central body. Indeed this material artifact is located just above the after-body and could be seen as an inlet perturbation and its influence on the unsteady base flow must be scrutinized. Note that the after-body flow around the nozzle is characterized by a large separation due to body geometry. In this sense, current flow configuration may approach other axisymmetric separating–reattaching flow configurations ([2,13] and references therein) previously investigated.

After a brief presentation of the experimental apparatus and the measurement method, the results are presented in two different parts. The first part is dedicated to the characterization of the wall pressure fluctuations and the associated integrated load. The classical Fourier analysis on both space and time is used to investigate the pressure signature on the nozzle for two different geometrical configurations. In the second part, the Proper Orthogonal Decomposition (POD) procedure is used to isolate specific energetic flow field that can be associated with side-load effect. Then, by coupling both wall pressure measurements and velocity field measurements, a statistical analysis is conducted to link the aerodynamic field to the wall pressure field and then to the force acting on the structure.

2. Experimental apparatus and measurement methods

2.1. Geometrical configurations

Over the years several wind tunnel experiments have been performed on an 86 cm long model (scale 1:60) of the Ariane 5 launcher (see Fig. 1) at the NLR (Dutch National Aerospace Laboratory) [1,9]. In previous works [10,17], different geometrical configurations including several free-stream Mach numbers have been investigated and studied in order to quantify the influence of the geometry on the flow. It has been shown that a relatively simple configuration without protuberances (tanks, tubes…) was able to represent the most important and critical phenomenon observed on the real geometry. This configuration (Fig. 2, left-hand side) will be discussed in this paper and will be referred as *Configuration A*.

The second configuration that is investigated in this study is geometrically close to *configuration A*, however the attachment device that connects the boosters to the main launcher body is removed. This is done to investigate their effect on the unsteady base flow since the attachment device (indicated in red in Figs. 1 and 2) is located directly upstream from the base and disturbs the flow in that location. Initially, this configuration has been designed to fit the geometry of the numerical simulations previously performed [23].

Fig. 2. Ariane 5 launcher model in the NLR wind tunnel. Left-hand side: *Configuration A*. Right-hand side: *Configuration B*. (For interpretation of the references to color in this figure, the reader is referred to the web version of this article.)

Table 1
Flow parameters in the wind tunnel configuration.

M_0	Total temperature	Free-stream temperature	Total pressure	Free-stream pressure	Dynamic pressure	U_0 ($m\,s^{-1}$)	(α, β)
0.8	311 K	275 K	100 200 Pa	65 740 Pa	29 444 Pa	266	(0, 0)

Table 2
Location of the 112 unsteady pressure transducers used to compute the integrated load.

Ring	X (mm)	Number of sensors	θ_0	$\Delta\theta$
1	−51.44	32	0	11.25
2	−46.44	16	0	22.5
3	−38.94	16	0	22.5
4	−30.94	8	22.5	45
5	−26.94	8	22.5	45
6	−20.56	8	22.5	45
7	−14.44	12	0	30
8	−7.44	12	0	30

In the absence of the attachment device, the boosters are no longer connected to the central body. To overcome this problem, a streamlined connection has been added further upstream to ensure the mechanical binding of the boosters. This new device is placed sufficiently far from the after-body in order to minimize its aerodynamic impact on the base flow. This configuration will be referred to *configuration B* for the rest of the paper (Fig. 2, right-hand side).

2.2. Wind tunnel and flow configurations

All the experiments are performed in the DNW HST transonic wind tunnel at a free-stream Mach number of 0.8. The wind tunnel model was placed at a zero degree angle of attack and zero degree yaw angle. An overview of the free-stream flow parameters is given in Table 1.

2.3. Wall pressure measurements

The most critical part of the geometry for side-load considerations is located on the engine nozzle and on the engine thermal protection. These parts are instrumented with a total of 112 unsteady pressure transducers distributed along 8 rings. The locations of pressure transducers are detailed in Table 2. Each pressure transducer records simultaneously the fluctuating wall pressure during a time duration of 2.56 s sampled at 12 800 Hz. During the acquisition, an anti-aliasing filter is applied on pressure signals with a cut-off frequency of 6400 Hz. Then, every spectral information will be available between $St = 10^{-4}$ and $St = 2$ (Strouhal number based on the central body diameter).

2.4. Particle image velocimetry measurements

Planar 2 component PIV measurements were carried out to capture the velocity field in the base region. Illumination was provided by a Litron LDY303HE Nd:YLF laser rated at 22.5 mJ/pulse at 1 kHz. The particle images are recorded by 2 LaVision HighSpeedStar 6 CMOS cameras having a resolution of 1024×1024 pixels. Camera 1 is equipped with a Nikkor 200 mm objective at $f_\# = 2$. The field of view of this camera is 92×92 mm (optical magnification is 0.22). The second camera has a Nikkor 180 mm objective at $f_\# = 2.8$ and the field of view is 110×100 mm^2 (optical magnification is 0.19). Liquid DEHS tracer particles are used in the experiments having a typical response time of 2 µs [21]. The particle concentration is estimated to be between 1 and 5 particles/mm^3. These PIV image pairs were recorded at a frequency of 2700 Hz and a total of $N_t = 2728$ velocity fields were obtained [21]. The measurements were performed in the plane orthogonal to the boosters (z-plane, see Fig. 3). The study primarily focuses on the unsteady part of the velocity, therefore the average velocity field is subtracted from every snapshot in order to obtain only the fluctuating part of the velocity field. For more details regarding the PIV experiments, the reader is referred to [10,21].

3. Integrated load characterization

Since it is very difficult and demanding to directly measure the unsteady loads on the nozzle [8], a first approach is to compute them from the unsteady wall pressure measurements.

3.1. Spatial characterization

Based on the synchronous wall pressure measurements providing a detailed description of spatio-temporally varying side loads, it is useful to get this information from the transducers by integrating the pressure along the nozzle as follows [16]:

$$\mathbf{F}(t) = \int_0^{2\pi} \int_0^{L} p(x,\theta,t) r(x) \mathbf{n}\, dx\, d\theta \equiv \sum_{i=1}^{N_c} p_i(t)\, \mathbf{dS}_i, \tag{1}$$

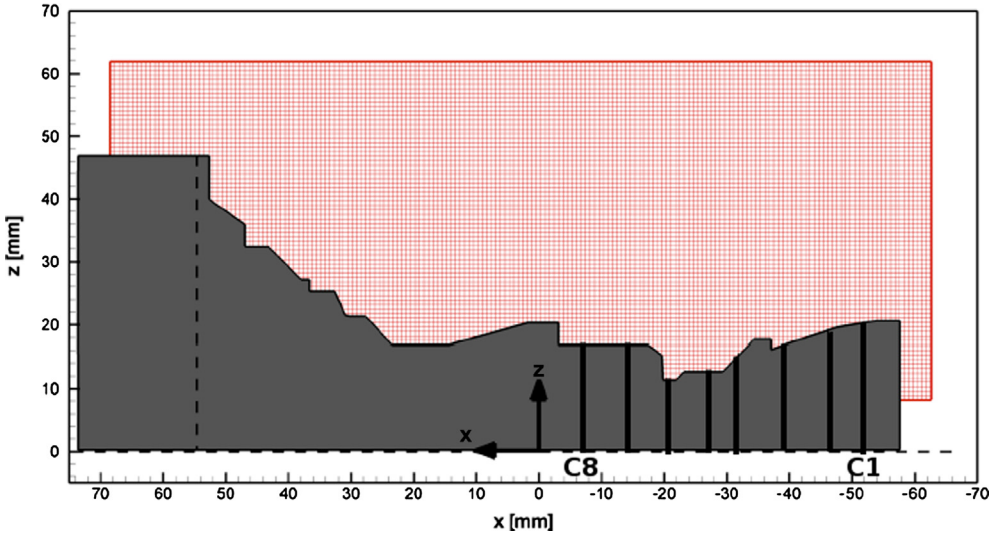

Fig. 3. PIV measurement (x, z) plane. The pressure transducer rings (from C1 to C8) are represented on the nozzle. (Parts of this figure are taken from [10].)

where dS_i is the elementary surface surrounding the ith sensor, N_c is the number of pressure transducers, L is the streamwise length, $r(x)$ is the nozzle radius at position x, $\mathbf{n}$ is the surface normal vector and $\equiv$ indicates the equivalence operator in discrete space. In this work, the integrated load refers to the integration of wall pressure load all around the 8 rings of sensors (that is both on the nozzle and on the engine thermal protection). They are then computed from the 112 corresponding pressure transducers (see Table 2).

From a modal point of view, the integrated load of Eq. (1) can be decomposed into azimuthal Fourier series, such as:

$$a_0 + \sum_{m=1}^{\infty} \alpha_m(t)\cos(m\theta) + \beta_m(t)\sin(m\theta). \tag{2}$$

As it was previously shown [16,17], the main contribution of the load is held by the two first Fourier modes, in such a flow configuration. Then, in this study, the integrated load is computed thanks to these two modes by combining Eqs. (1) and (2) to get:

$$\mathbf{F}_m(t) = \sum_{i=1}^{N_c} p_i(t)\, dS_i \left[\cos(m\theta)\mathbf{y} + \sin(m\theta)\mathbf{z}\right], \tag{3}$$

where $\mathbf{y}$ and $\mathbf{z}$ are unitary vectors defined in Fig. 1, dS_i is the elementary surface surrounding sensor i (see [16]) and m refer to the Fourier mode number (1 or 2). From a structural point of view, F_1 and F_2 have a different effect on the nozzle. These effects are shown schematically in Fig. 4 and correspond exactly to the structural modes of the nozzle [9,20,25].

3.2. Spectral characterization

Thus by using the approach outlined above the temporal variation of the load becomes available which now allows to perform a Fourier analysis. The Power Spectral Densities (PSD) of the loads are represented as a function of the Strouhal number, $St = fU_0/D$, in Fig. 5 for both configurations. The following notations are used: G_m^y and G_m^z correspond to the PSD of $\mathbf{F}_m.\mathbf{y}$ and $\mathbf{F}_m.\mathbf{z}$ respectively. First, for *configuration A*, G_1^y is characterized by a peak around $St = 0.2$ while G_2^y and G_2^z exhibit a broad-band load around $St = 0.5$. These frequency repartitions fit those of the nozzle mechanical modes and lead to a strong fluid structure interaction. Furthermore, it is observed that *configuration B* (where the attachment device is removed) induces a weaker $\mathbf{F}_1$ load than the one observed in flow *configuration A*. This result demonstrates that the attachment device has a dramatic effect on the unsteady load acting on the nozzle. However, these effects are less pronounced for the $\mathbf{F}_2$ load and particularly for G_2^z (Fig. 5, right-hand side, red color representation).

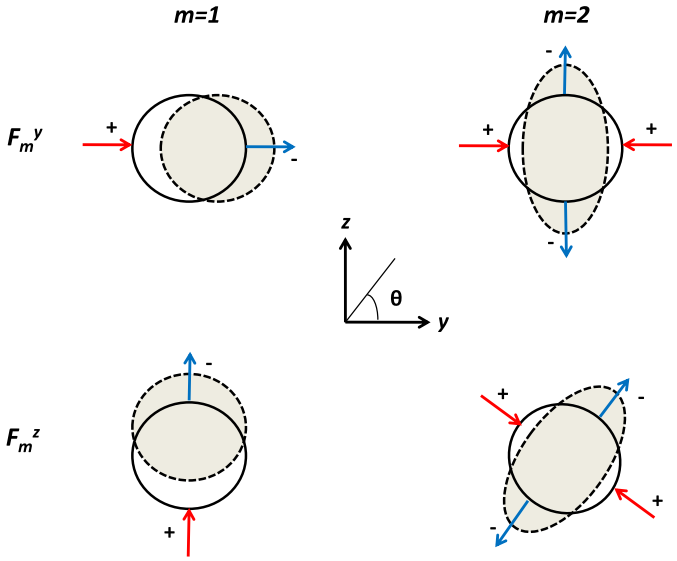

Fig. 4. Effect of the F_m^y and F_m^z load on the nozzle structure for $m = 1$ and $m = 2$. The $m = 1$ load is often referred as the pendulum load and the $m = 2$ load as the ovalization load. Gray pictures indicate the next structure location (or deformation) under F_1 (or F_2) load effect.

These first global differences in the unsteady load induced by two different geometries are of primary importance for the understanding of the fluid structure interaction and its origins should be sought in the unsteady flow organization. Therefore a further investigation of the flow field is necessary. Some previous works have shown that a more local Fourier analysis of the wall pressure field also gave relevant information about load effects [9,17]. The purpose of this work is mainly related to establish a link between the wall pressure measurements and flow velocity measurements to investigate the aerodynamic flow which is more correlated to the side load effect. For such a purpose, an analysis based on the Proper Orthogonal Decomposition (POD) is proposed in the following.

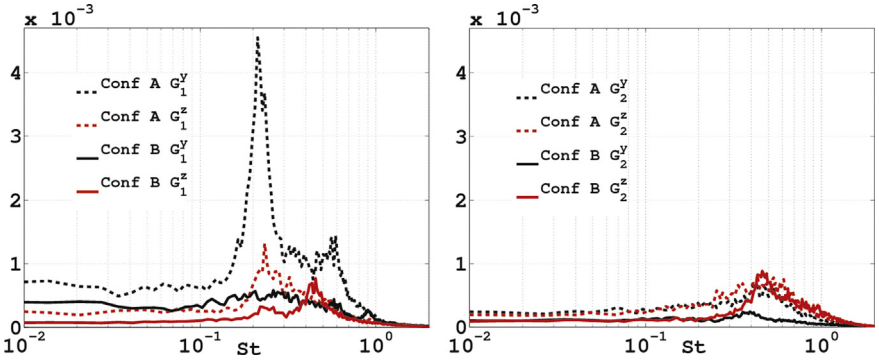

Fig. 5. PSD of the F_1 load (left-hand side) and of F_2 (right-hand side), projected onto z-axis (red color) and onto y-axis (black color). Dashed lines are for *configuration A* and the filled line for *configuration B*. These curves are voluntarily set with the same arbitrary units. (For interpretation of the references to color in this figure, the reader is referred to the web version of this article.)

4. POD investigation of the flow field

Proper Orthogonal Decomposition (POD) is an efficient statistical technique to provide an optimal basis for extracting the spatial structure of the most energetic fluctuations in the flow field in an average sense [14]. Such a method is particularly well suited for the detection and the extraction of large-scale energetic coherent flow structure present in turbulent flow [4,5,12]. Furthermore, Hudy et al. [13] demonstrated the ability of POD to determine the dominant modes in the pressure signature from wall pressure measurements performed in a separating–reattaching flow region downstream of an axisymmetric backward-facing step at low Reynolds number.

In this section, the Proper Orthogonal Decomposition is used to characterize the most energetic part of the flow and its contribution to the integrated load. Ultimately, POD is used to achieve relevant information about the pressure–velocity correlations in the flow.

4.1. Brief recall of mathematical concept

Briefly, the goal of the POD technique is to find the optimal representation of the field realizations, which leads to a Fredholm integral equation:

$$\int_S R\left(\mathbf{X}, \mathbf{X}'\right)\phi^{(n)}\left(\mathbf{X}'\right) d\mathbf{X}' = \lambda^{(n)}\phi^{(n)}(\mathbf{X}), \tag{4}$$

where $\mathbf{X}$ indicates the space variable and $R(\mathbf{X}, \mathbf{X}')$ refers to the time averaged two point spatial correlation tensor of the pressure field. In this equation, ϕ denotes the spatial orthogonal eigenfunctions and λ is the corresponding eigenvalue. Such an equation provides a finite discrete number of a POD eigenfunctions, $\phi^{(n)}$ with n varying from 1 to N_{mod} which is the total number of POD modes corresponding to the rank of the spatial correlation matrix. Such a POD application is called the classical version of POD introduced by Lumley [15]. When dealing with a larger number of grid points than the number of available instantaneous flow field, to reduce the computational effort involved in solving the above eigenvalue problem, it is preferable to use the snapshot version of POD introduced by Sirovich [22]. In this case, the kernel of the Fredholm equation is based on a spatial averaging and the eigenfunctions resulted from the snapshot formulation are now temporal ones, $a^{(n)}(t)$. Both POD procedures lead to a similar flow variable decomposition:

$$p(\mathbf{X}, t) = \sum_{n=1}^{N_{mod}} a^{(n)}(t)\phi^{(n)}(\mathbf{X}), \tag{5}$$

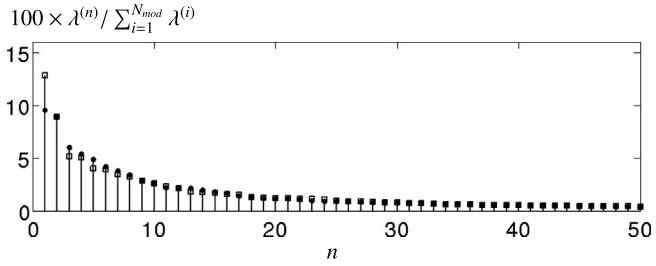

Fig. 6. Percentage of the total energy contained in each of the 50 first pressure modes. White squares are related to *configuration A* and black circles to *configuration B*.

satisfying $\overline{a^{(n)}(t)a^{(m)}(t)} = \delta_{nm}$, with δ the Kronecker symbol, and $\langle \Phi^{(n)}\Phi^{(m)} \rangle = \lambda^{(n)}\delta_{nm}$. N_{mod} is the rank of the correlation matrix R. Note that when dealing with wall pressure field, $\mathbf{X}$ is related to (x, θ) variables.

The interest of such flow decomposition is that the first few POD modes contain the significant part of the flow energy and the unsteady flow field can be represented by a linear combination of a relatively small number of temporal and spatial eigenfunctions. Using the POD mode orthogonality and its non-correlation, it is then possible to extract some physical flow mechanisms, especially when dealing with the first energetic POD modes. Conversely, the POD mode residue may be interpreted with difficulty due to less energetic POD modes can be erroneously contaminated with measurements errors [7] or with poorly statistical convergence [11].

Such an application allows the identification of the main energetic contribution of the flow helping in interpreting the side-load effect.

4.2. Pressure modes investigation

4.2.1. Wall pressure modes

The classical POD procedure is applied to the unsteady fluctuating pressure field (deduced from the Reynolds decomposition) obtained in each flow configuration (A and B). In each test case, it leads to $N_{mod} = 112$ POD modes corresponding to the number of available wall pressure signals. Time histories of the wall pressure field can be then described through POD analysis as series of orthogonal spatial functions and uncorrelated temporal functions (see Eq. (5)).

Fig. 6 displays the distribution of eigenvalues for the first 50 eigenmodes. It is observed that the eigenvalues decrease very rapidly for the first 15 modes. Indeed, each POD mode number superior to 15 contains less than 2% of the total energy. The first two POD modes computed from *configuration A* represent 23% of the total energy whereas they represent only 16% when dealing

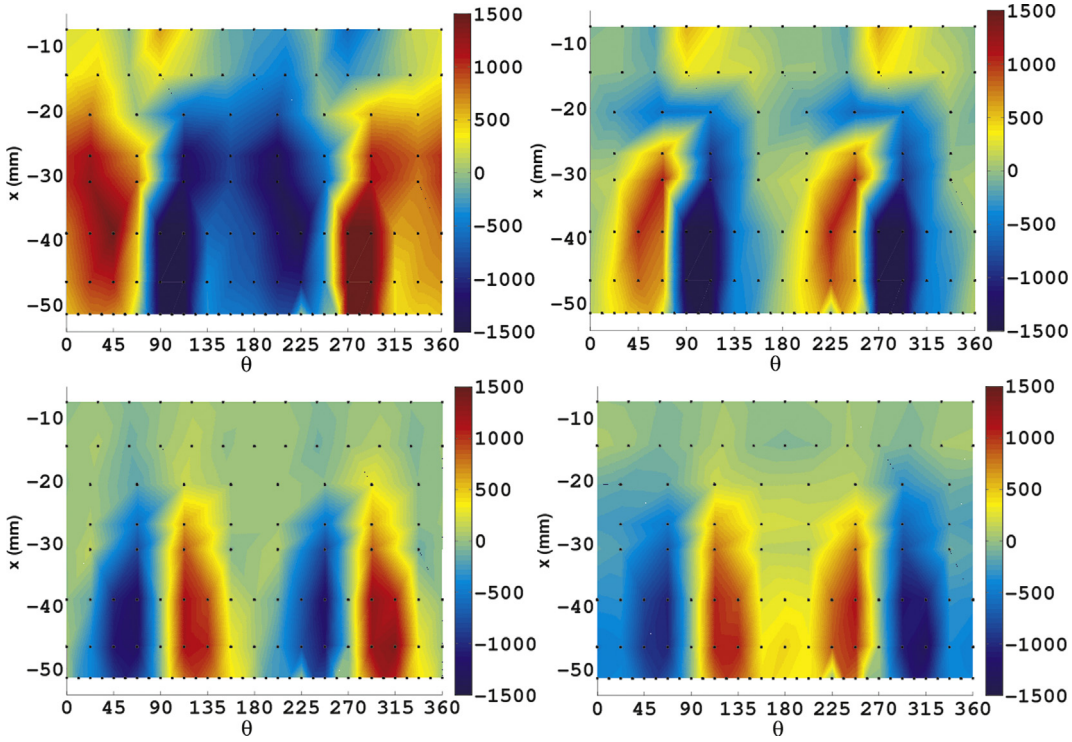

Fig. 7. First (left) and second (right) POD modes of the pressure. *Configuration A* (top) and *configuration B* (bottom).

with *configuration B*. This main difference is held by the high energy content of the first mode extracted from flow *configuration A*.

The first two spatial pressure modes are shown in Fig. 7. This figure displays the quantity $\sqrt{\lambda^{(n)}}\phi^{(n)}(x,\theta)$, for n varying from 1 to 2. From these results, the following comments can be made:

- The first pressure mode of *configuration A* induces a positive pressure contribution on parts A1 and B1 ($0 < \theta < 90$ and $270 < \theta < 360$) and a negative contribution on parts A2 and B2 (see Fig. 1, left-hand side). It then mainly contributes to the pendulum structural excitation on y-axis displayed in Fig. 4. That corresponds to a local displacement of the nozzle and suggests a contribution to the F_1^y load.
- The second pressure mode of *configuration A* induces a positive pressure contribution on parts A1 and B2 ($0 < \theta < 90$ and $180 < \theta < 270$) and a negative contribution on parts A2 and B1 (see Fig. 1, left-hand side). They then mainly contribute to the ovalization structural excitation on z-axis displayed in Fig. 4 (right-hand side). That corresponds to a local deformation of the nozzle and suggests a contribution to the F_2^z load.

These observations indicate that the first two pressure POD modes contain the information about the load effects of the pressure on the nozzle.

Conversely, when regarding *configuration B* results, the contribution to the F_1^y load is held by the second POD mode and the contribution to F_2^z is held by the first POD mode. This indicates that the contribution to F_1^y (displacement of the nozzle) is less energetic for *configuration B* compared to results deduced from *configuration A*.

High order POD modes are difficult to interpret due to their associated less energetic content and their spatial distribution which do not correspond to particular loading effect [18]. They are mainly related to small energetic events associated with the three-dimensional nature of the flow field interacting with the wall.

This similarity between pressure POD modes and load effect suggests a strong similarity between $a^{(n)}(t)\phi^{(n)}(\mathbf{X})$ (Eq. (5)) and $p_i(t)\cos(m\theta)\,dS_i$ (Eq. (3)). To valid such a statement, the integrated load is now computed using Eq. (3), substituting $p_i(t)$ by its projection onto the POD basis.

4.2.2. POD mode loading investigation

Using the POD flow partitioning, the contribution of the POD modes to the unsteady loads computed with Eq. (3) is investigated. Let us define $\{F_m\}_k^l$ as the unsteady load that is induced by the wall pressure field p_k^l which is projected onto the POD modes from k to l as:

$$p_k^l(\mathbf{X},t) = \sum_{n=k}^{l} a^{(n)}(t)\phi^{(n)}(\mathbf{X}). \tag{6}$$

For instance, $\{F_m\}_1^1$ represents the load induced by the first POD mode of the pressure and $\{F_m\}_3^{112}$ represents the load induced by the pressure field projected onto POD modes from 3 to 112. Figs. 8 and 9 display the PSD of $\{F_m\}_1^1$, $\{F_m\}_2^2$ and $\{F_m\}_3^{112}$ for *configuration A* and *B* respectively. In these figures, only the most energetic modes contribution is represented (F_1^y and F_2^z) and the reference PSD of $F_m = \{F_m\}_1^{112}$ is also plotted for comparison.

The analysis of *configuration A* results shows that the PSD of the first pressure POD mode ($\{G_1^y\}_1^1$) strongly contributes to G_1^y by reproducing the main frequency shape of the total PSD load. Similarly, the PSD of the second pressure POD mode ($\{G_2^z\}_2^2$) strongly contributes to G_2^z. These results indicate that the POD mode number 1 contains information about the $m = 1$ Fourier mode and the POD mode number 2 contains information about the $m = 2$ Fourier mode. This is in agreement with the previous analysis (see Section 4.2.1). Moreover, it is also noticeable that for *configuration A* the first (resp. second) pressure POD mode does not contribute to $\mathbf{F}_2$ (resp. $\mathbf{F}_1$). They are uniformly zero value in each case. The residual POD modes (from 3 to 112) seem to have a higher contribution in $\mathbf{F}_2$ than in $\mathbf{F}_1$. It suggests that small energetic events are more favorable to a local deformation of the nozzle ($m = 2$ load in Fig. 4).

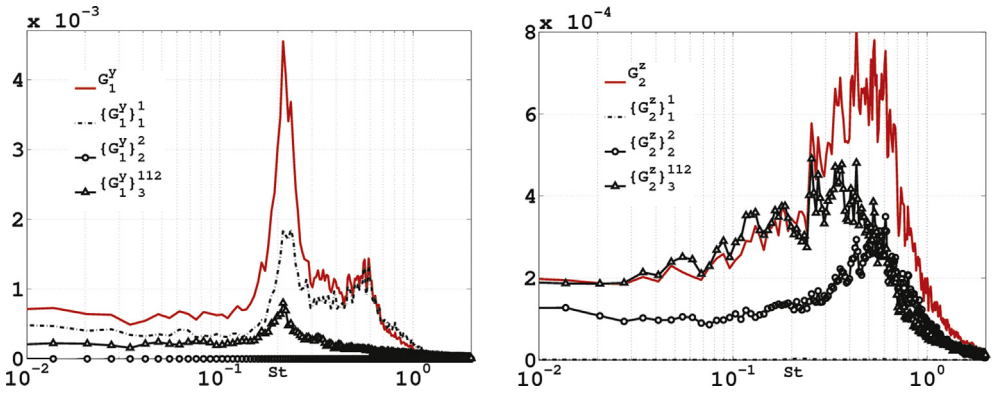

Fig. 8. Contribution of the POD modes to the PSDs of F_1^y (left-hand side) and to F_2^z (right-hand side) for *configuration A*.

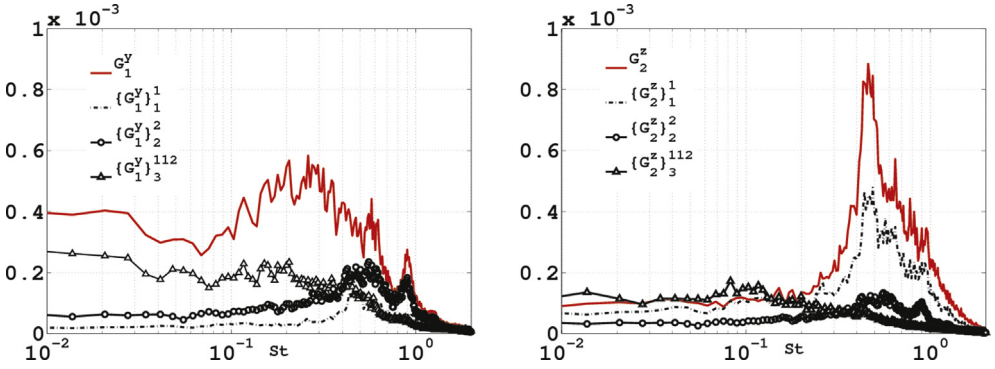

Fig. 9. Contribution of the POD modes to the PSDs of F_1^y (left-hand side) and to F_2^z (right-hand side) for *configuration B*.

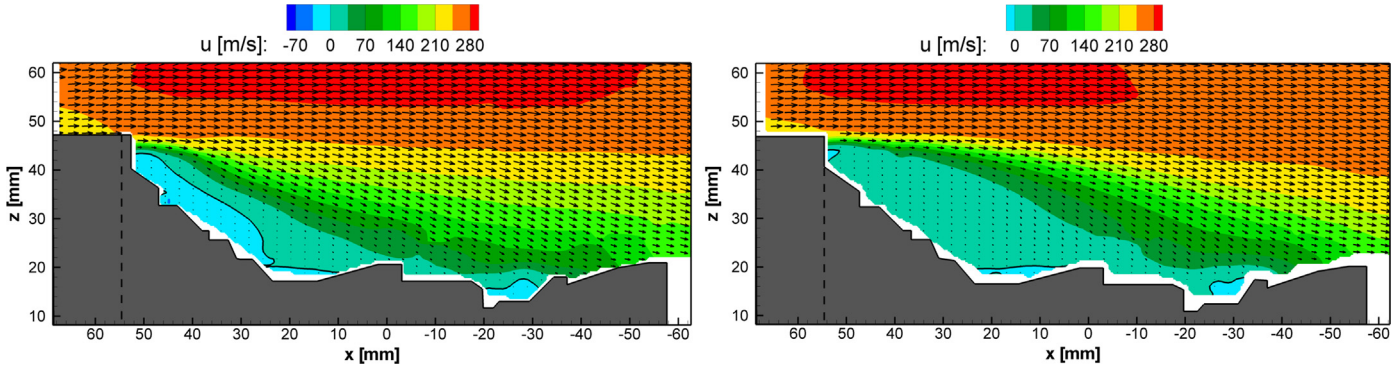

Fig. 10. Mean longitudinal velocity component U. *Configuration A* (left-hand side). *Configuration B* (right-hand side).

When regarding *configuration B* results, one observes that the PSD contribution of the POD modes is also in agreement with the previous analysis (see Section 4.2.1): the first POD mode is linked to $\mathbf{F}_2$ and the second POD mode is linked to $\mathbf{F}_1$. As opposed to *configuration A* results, the first two POD modes have always a non-zero contribution to F_1 and F_2 loads. In a similar way, residual modes give a contribution to both $\mathbf{F}_1$ and $\mathbf{F}_2$.

Thus, the application of Proper Orthogonal Decomposition to the wall pressure field has highlighted that the main phenomenon responsible for the unsteady load acting on the nozzle is mainly contained in the first two energetic POD modes. For such a present flow configuration, POD is then a powerful mathematical procedure to isolate the physical contribution of the wall pressure field to the unsteady load. The main difference between both configurations holds in the structured and organized phenomena which are perfectly identified for the *configuration A*, and less stressed for the *configuration B*. Such pressure POD mode investigations underline that different load effect occurs as a function of the flow configuration. In this sense, it is necessary to examine the external velocity field to better understand the differences in both configurations.

4.3. External velocity field investigation

4.3.1. Global mean analysis

Based on the available $N_t = 2728$ PIV velocity vectors, the mean flow field is computed and displayed in Fig. 10 for both *configurations: A* (left-hand side) and *B* (right-hand side). Only the mean streamwise velocity component is represented to investigate the recirculation area. The presence of the attachment device in *configuration A* induces a smaller recirculation bubble than the one observed in *configuration B*. Indeed, the attachment device obstructs the flow in the vicinity of its detachment region and thus has important effects on the recirculation bubble. The size of this area determines the length of the reattachment region and thus the intensity of the integrated load on this part. In this sense, *configuration B* exhibits a larger recirculation bubble suggesting a less

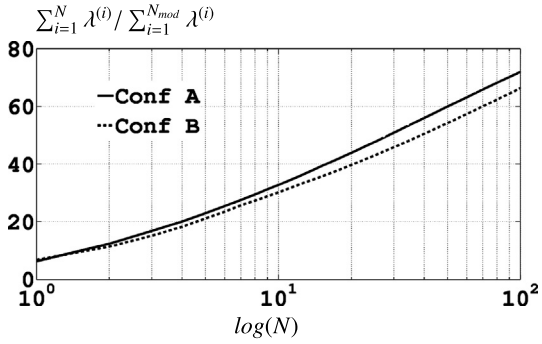

Fig. 11. Evolution of the cumulated percentage of the total energy with the number of modes.

prominent impact of the flow on the nozzle. These assessments are to be linked with the streamwise repartition of the pressure POD modes (see Fig. 7) where pressure fluctuations are observed on the thermal protection ($-10 < X < -20$) for *configuration A* but disappear for *configuration B*.

In the current experiments the PIV acquisition frequency was limited to 2700 Hz which compares to a Strouhal number of $St = 1.1$. This means that all frequencies present in the flow field above $St = 1$ will be aliased and will distort any results coming from spectral analysis. Since for the current flow field there still is quite some activity above this limit, a spectral analysis is not possible.

In this sense, despite the aliasing problem, the Proper Orthogonal Decomposition may be an alternative solution for current statistical investigation. It provides reliable information about the coherent structures of the velocity field. In Eq. (4), $R(\mathbf{X}, \mathbf{X}')$ refers now to the time averaged two point spatial correlation tensor of the velocity field and $\mathbf{X}$ is referred to the spatial variables (x, z). Thus POD velocity mode computation is not corrupted by the low frequency used for PIV sampling.

4.3.2. POD analysis of the velocity field

A snapshot vectorial POD is performed to elucidate the large-scale flow structure present in the turbulent flow. That leads to obtain $N_{mod} = 2728$ POD modes corresponding to $N_t = 2728$ available instantaneous PIV images of the fluctuating velocity field.

Fig. 11 shows the cumulative flow energy according to the whole available POD modes. It provides a number of modes needed to achieve a given percentage of the total turbulent kinetic energy. Epps and Techet [7] showed that beyond a certain number of modes obtained from PIV data, the observed energy was only due to a random noise of the data. This criterion indicates that for current PIV data, the POD modes beyond 500 do not have to be taken into account. According to Fig. 11, 70% of the energy is contained in the first 100 modes. The small energetic content in the first POD modes traduces the high turbulent character of the flow.

Fig. 12 displays the spatial characteristics of the first four velocity modes, $\sqrt{\lambda^{(n)}}\phi^{(n)}(x, z)$. Firstly, *configuration A* exhibits larger and more energetic modes traducing a more organized flow. This is also directly related to the energy content of POD modes (see Fig. 11). In both configurations, the first 4 POD modes are capable of well representing the large-scale unsteadiness of the flow field.

Secondly, by looking at positive and negative velocity regions, the spatial structure of the modes in both configurations is related to a fluctuation of the recirculation bubble and the reattachment area. This suggests that these POD modes are related to the reattachment region and should be linked with the load acting on the nozzle. For a more in depth discussion on the relation between the dynamic behavior of the separated region and shear layer and the POD modes, see [21].

The POD application to the wall pressure and the flow velocity shows that the main phenomenon responsible for the unsteady loads acting on the nozzle is held by a very small number of POD modes representing large and energetic structures. Therefore, the correlation between the wall pressure signature and the flow structure of the velocity field has to be strengthened thanks to a cross-correlation analysis.

5. Analysis of the cross correlation between the wall pressure and velocity field

In the present study, we focus on the physical origins of the unsteady loads acting on the nozzle. Thus, a statistical analysis based on the determination of correlations between the velocity field and the wall pressure data seems necessary. Previous analyses coupling surface pressure measurements and Particle Image Velocimetry (PIV) measurements have been already performed to

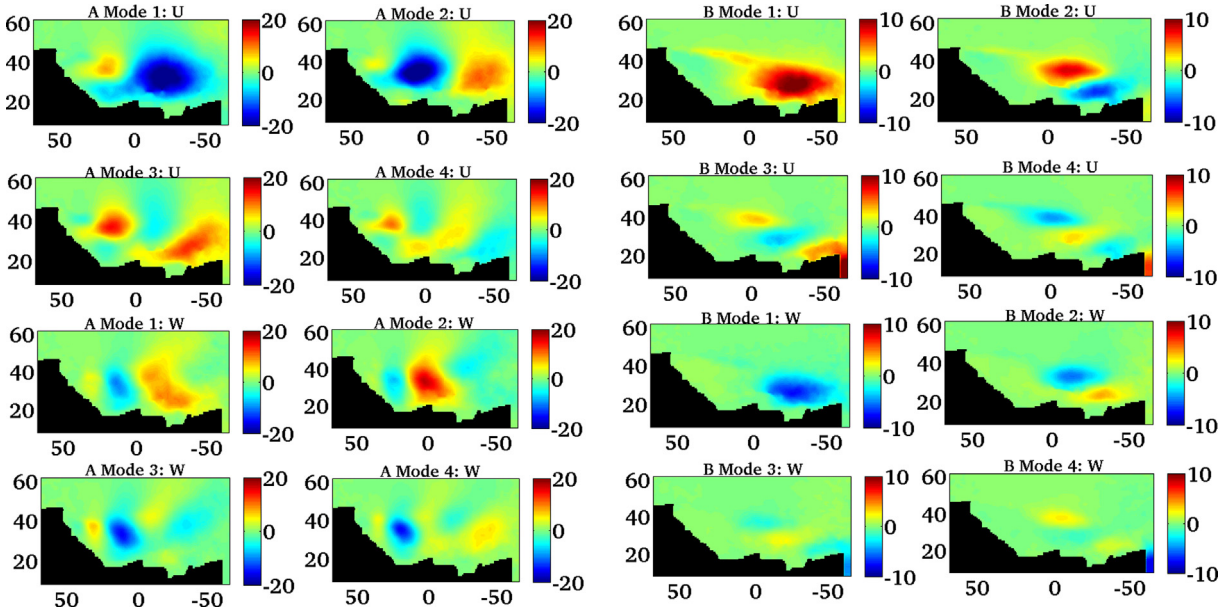

Fig. 12. Representation of the first 4 velocity POD modes for *configuration A* (left-hand side) and *configuration B* (right-hand side). Color scale displays the quantity $\sqrt{\lambda^{(n)}}\phi^{(n)}(x, z)$. (For interpretation of the colors in this figure, the reader is referred to the web version of this article.)

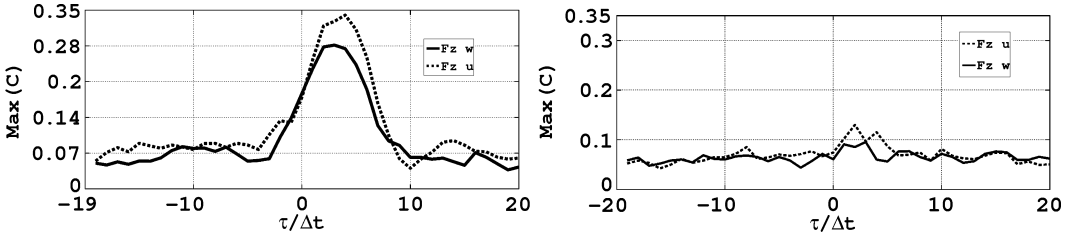

Fig. 13. Evolution of the maximum correlation $\max[C^{u}_{F_1^z}(\mathbf{X})]$ (dashed lines) and $\max[C^{w}_{F_1^z}(\mathbf{X})]$ (solid lines) with the parameter $\tau/\Delta t$. *O* value correspond to the synchronization ignition. Left: *Configuration A*. Right: *Configuration B*.

estimate the dominant flow structures best correlated with surface pressure signals [13,19]. Moreover, as it has been previously done for investigating the flow structures involved in the sound generation [4,6] or involved in the wall of a backward-facing step [13], a statistical correlation analysis provides some useful information about the external flow region which exhibits the highest correlation with the surface pressure and then with the side-load force. In the references cited above, such statistical analysis was coupled to POD mode flow decomposition to bridge between aerodynamic event and sound generation or wall pressure respectively. Then, in the following, similar statistical analyses are successively performed.

5.1. Definition of cross-correlation variables

A crucial point is to understand if some pressure modes are linked to a particular flow structure and where does this link come from. The idea is to use here not only the classical correlation techniques but also the POD analysis in order to extract the relevant information from pressure and velocity fields, respectively. As a first investigation, the basic correlation is defined by:

$$C(\mathbf{X}', \mathbf{X}) = \overline{p(\mathbf{X}', t).U(\mathbf{X}, t)}, \tag{7}$$

where an overbar denotes the time averaging operator. This definition supposes that $p(\mathbf{X}', t)$ and $U(\mathbf{X}, t)$ are known at the same moments. Recall that $\mathbf{X}'$ and $\mathbf{X}$ associated with wall pressure field and velocity field correspond to (x, θ) and (x, z) variables respectively. During the acquisition, pressure and velocities are synchronized in order to have the same starting point for pressure and velocity signals. However, the pressure sampling frequency is 12.8 kHz and the velocity sampling frequency is 2.7 kHz. Thus, the only way to get a reliable correlation is to sub-sample the pressure signal and to interpolate this signal on the velocity time base. Then we obtain pressure and velocity signals of one second sampled at 2700 Hz. It is important to note here that no pressure filter is applied in this procedure. That allows to keep the overall energy of the pressure signal. Indeed, as we do not proceed to any Fourier transform of the pressure, but only to the correlation computation, the sub-sampling has only small effects on the observed overall correlation values.

The first step consists in choosing which wall pressure field has to be correlated to the exterior aerodynamic flow field. Such choice may be complex and quite dependent to available database. To avoid any misinterpretation, it is proposed to investigate directly the link between the velocity field and the global integrated load $F_m^z(t)$. In this sense, in Eq. (7) the wall pressure signal is replaced by $F_1^z(t)$ or $F_2^z(t)$, where $F_m^z(t)$ is the load projection in the z-axis (PIV plane) integrated with the sub-sampled pressures. This method is well adapted to the current aim of this work, that is to find the exterior flow field which is mainly correlated to the unsteady load of the nozzle. In the following, the correlation will be written with subscript and superscript to distinguish the correlated quantity. Then, $C^{u}_{F_m^z}(\mathbf{X})$ represents the correlation between the z-load and the U velocity component. The new correlation only depends on $\mathbf{X}$ because the space-integrated quantity F_m^z does not depend on space.

Furthermore, in order to handle a time delay between the instantaneous velocity field and its local effects on the load, it is necessary to consider a parameter τ into the correlation. This last parameter is introduced in the pressure signal by substituting $F_m^z(t)$ by $F_m^z(t+\tau)$. Then, the maximum of correlation obtained with different value of τ is computed and displayed in Fig. 13. It shows that a delay of 4 time steps induces the maximum of correlation. This corresponds to a time delay of 0.31 ms and a space interval of 42.5 mm based on a convection speed of $U_0/2 \sim 136$ m/s. The maximum of correlation is observed in both cases between the z-load and the U-component of the velocity. In the following, all the correlations are computed with $\tau = 4\Delta t$.

Another way to increase the accuracy of the cross-correlation computation is to use the physical assessments exposed in the modal overview of the flow.

Indeed, as shown previously (see Sections 4.2 and 4.3.2), the most energetic POD modes of the pressure and the velocity contain the most interesting physics of the flow under investigation. Thus a modified computation of the correlation is defined following Eq. (6):

$$\left[C^{u}_{F_m^z}\right]^{l}_{k}(\mathbf{X}) = \overline{\left\{F_m^z\right\}^{k}_{1}(t).U^{l}_{1}(\mathbf{X}, t)}, \tag{8}$$

where $U^{l}_{1}(\mathbf{X}, t)$ is the projection of the velocity signal onto the first l POD modes. Then the parameter k refers to the number of wall pressure POD modes considered and the parameter l to the number of velocity modes. According to the results of Section 4.2.1, the parameter k is fixed to 2 in the following. Conversely, the selection of the number l related to velocity POD modes is more complex. To determine this number, the evolution of the maximum of $[C^{u}_{F_m^z}]^{l}_{k}$ is plotted versus l in Fig. 14.

It clearly indicates that for $l > 5$, the maximum of correlation, $[C^{u}_{F_m^z}]^{l}_{k}$ remains globally the same. Then, in the following, the parameter l is set to 5.

5.2. Results and discussion

Fig. 15 displays the spatial representation of $[C^{u}_{F_m^z}]^{5}_{2}$ and $[C^{w}_{F_m^z}]^{5}_{2}$ for each the Fourier modes under investigation ($m = 1$ and $m = 2$). The first two lines of plots compare directly results arising from *configuration A* and *configuration B*.

By focusing on *configuration A* results (Fig. 15), it is observed that the unsteady loads on the nozzle (F_1^z and F_2^z) are mainly correlated to highly energetic structures of the flow. However the discrimination of F_1^z and F_2^z is not possible in this case. Indeed, as stated in Section 3.1 the spatial Fourier modes are linked to the azimuthal repartition of the pressure, which cannot be accessed due to the orientation of the PIV measurement plane. Nevertheless, the results display that there is a significant correlation between the loads F_1^z and F_2^z and the velocity field as is expected.

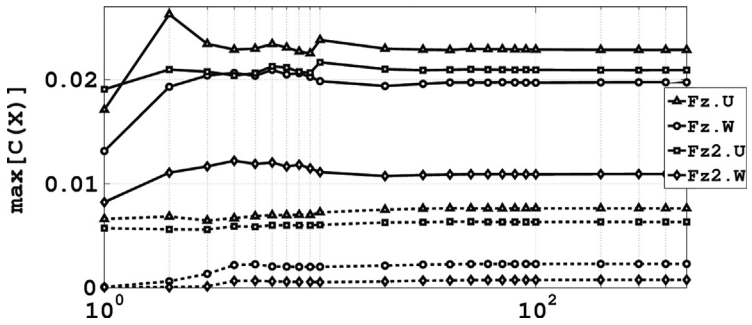

Fig. 14. Evolution of the maximum correlation $[C^u_{F^z_m}]^l_k$ with parameter l. Solid lines: *Configuration A*. Dashed lines: *Configuration B*.

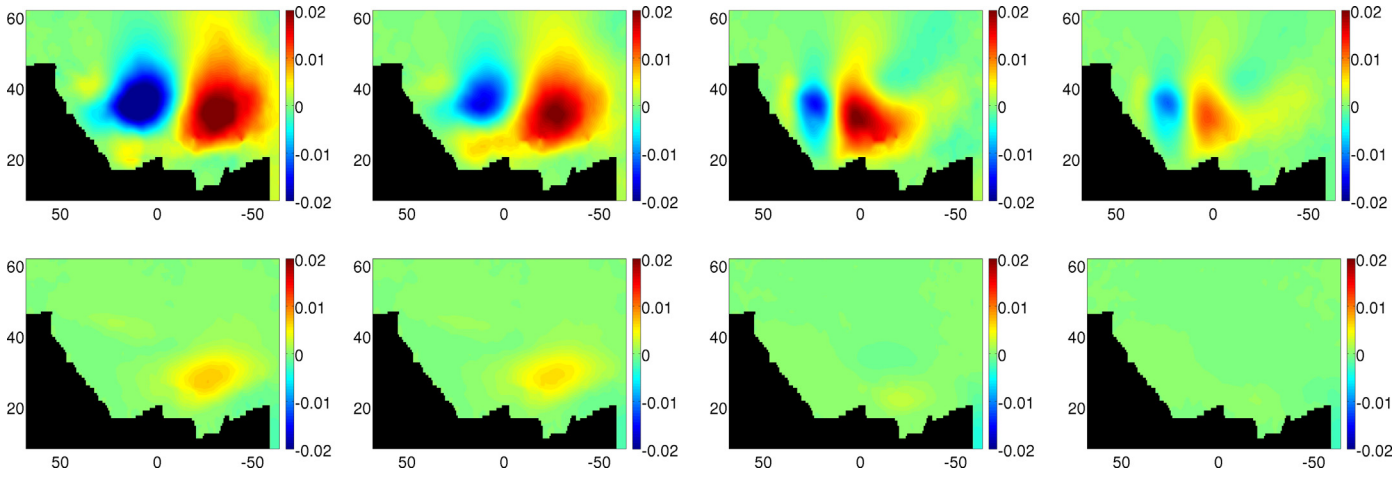

Fig. 15. Correlation between z-load and velocity components. From left to right: $[C^u_{F^z_1}]^5_2(\mathbf{X})$, $[C^u_{F^z_2}]^5_2(\mathbf{X})$, $[C^w_{F^z_1}]^5_2(\mathbf{X})$ and $[C^w_{F^z_2}]^5_2(\mathbf{X})$. First line: *Configuration A*. Second line: *Configuration B*.

Then, the high correlation is spread over a large area located around the 2 main velocity POD modes (see Fig. 12). This indicates that the dynamic of these 2 modes strongly influences the pressure distribution along the nozzle and consequently the amplitude of the unsteady load.

Finally, the whole cross-correlation analysis allows to demonstrate that the level of cross correlation from *configuration A* always exceeds the one deduced from *configuration B* (see Figs. 13 and 14). The same can be concluded from Fig. 15. These results must be seen as a further interpretation of the influence of the attachment device. *Configuration A* with the attachment system gives rise to a perturbed flow containing large and coherent structures which are convected favorably to the nozzle inducing a strong correlation between the velocity field and the unsteady load. *Configuration B* without the attachment system exhibits a displacement of the mean reattachment point on the nozzle inducing a weaker correlation between the unsteady load and the velocity field.

6. Conclusion

The unsteady aerodynamics of the Ariane 5 after-body is the home of complex phenomenon. Comparison between two different geometrical configurations is an efficient way to understand the influence of some artifacts on the base flow. In this study, the influence of the attachment device onto the side-load effect has been scrutinized.

A physical analysis of the associated flows has shown that the attachment device was inducing an unsteady load characterized by energetic and coherent structures with a frequency shape similar to that of the nozzle structural modes. The Proper Orthogonal Decomposition has been applied to the wall pressure and external velocity fields. The similarity between the spatial Fourier modes and POD modes for the wall pressure field has strengthened the choice of the Proper Orthogonal Decomposition for a global analysis of the flow. It has been shown that the main physics was governed by two particular pressure modes and five main velocity modes. The study of the pressure–velocity correlations has highlighted the relationships between the main modes of the velocity field and the observed unsteady load on the nozzle. This modal analysis has confirmed the structural influence of the attachment device and its contribution to the structural dynamic load. The main results emphasized that the presence of the attachment system generates a global shedding phenomenon growing in the early detaching flow with a characteristic frequency of $St = 0.2$. Then, turbulent structures represented by the first velocity POD modes are convected in the rear-part of the nozzle and impact the mechanical structure, inducing a broad-band load.

The results of this paper are based on the wall pressure fluctuation measurements and 2D PIV investigations. It is important to note that a full understanding of the highlighted phenomena will rely on a fully 3D analysis based on the time-resolved azimuthal repartition of the velocity fluctuations. In particular, the discrimination between the spatial Fourier modes of the pressure and their correlation to the upstream flow will only be possible with some knowledge of the frequential or azimuthal repartition of the velocity. This analysis will be feasible with heavy and accurate numerical simulations or improved PIV techniques.

Acknowledgements

The present research was performed in the framework of the ESA TRP Unsteady Subscale Force Measurements within a Launch Vehicle Base Buffeting Environment [10] financed by the Eu-

ropean Space Agency. The prime contractor of this project is DLR (Germany) with membership of NLR (Netherlands), TU-DELFT (Netherlands), EADS-Astrium (France), ONERA (France) and CNES (France).

References

[1] S. David, S. Radulovic, Prediction of buffet loads on the Ariane 5 afterbody, in: 6th Symposium on Launcher Technologies, Munich, Germany, 2005.
[2] S. Deck, P. Thorigny, Unsteadiness of an axisymmetric separating–reattaching flow: Numerical investigation, Phys. Fluids 19 (2007) 065103, 20 pp.
[3] D. Deprés, P. Reijasse, J. Dussauge, Analysis of unsteadiness in afterbody transonic flows, AIAA J. 42 (12) (2004) 2341–2550.
[4] P. Druault, X. Gloerfelt, T. Mervant, Investigation of flow structures involved in sound generation by two- and three-dimensional cavity flows, Comput. Fluids 48 (1) (2011) 54–67.
[5] P. Druault, P. Guibert, F. Alizon, Use of proper orthogonal decomposition for time interpolation from PIV data, Exp. Fluids 39 (2005) 1009–1023.
[6] P. Druault, M. Yu, P. Sagaut, Quadratic stochastic estimation of far field acoustic pressure with coherent structure events in a 2D compressible plane mixing layer, Int. J. Numer. Methods Fluids 62 (2010) 906–926.
[7] B. Epps, A. Techet, An error threshold criterion for singular value decomposition modes extracted from PIV data, Exp. Fluids 48 (2010) 355–367.
[8] F. Garçon, J. Drevet, Unsteady load measurements on the main engine nozzle of the Ariane 5 launch vehicle, in: Third European Symposium on Aerothermodynamics for Space Vehicles, ESA, ESTEC, Noordwijk, The Netherlands, 1998, p. 623.
[9] E. Geurts, Steady and unsteady pressure measurements on the rear section of various configurations of the Ariane 5 launch vehicle, in: 6th Symposium on Launcher Technologies, Munich, Germany, 2005.
[10] K. Hannemann, H. Ludeke, J.-F. Pallegoix, A. Ollivier, H. Lambare, J. Maseland, E. Geurts, M. Frey, S. Deck, F. Schrijer, F. Scarano, R. Schwane, Launch vehicle base buffeting: Recent experimental and numerical investigations, Tech. rep., Unsteady Subscale Force Measurements within a Launch Vehicle Base Buffeting Environment, 2011.
[11] A. Hekmati, D. Ricot, P. Druault, About the convergence of POD and EPOD modes computed from CFD simulation, Comput. Fluids 50 (2011) 60–71.
[12] P. Holmes, J. Lumley, G. Berkooz, Turbulence, Coherent Structures, Dynamical Systems and Symmetry, Cambridge Monograph on Mechanics, Cambridge University Press, 1996.
[13] L. Hudy, A. Naguib, W. Humphreys, Stochastic estimation of a separated-flow field using wall-pressure-array measurements, Phys. Fluids 19 (2007) 024103.
[14] R. Humble, F. Scarano, B. van Oudheusden, Unsteady flow organization of compressible planar base flows, Phys. Fluids 19, http://dx.doi.org/10.1063/1.2739411.
[15] J. Lumley, The structure of inhomogeneous turbulent flows, in: Yaglom, Tatarsky (Eds.), Atm. Turb. and Radio Wave Prop., Nauka, Moskva, 1967, pp. 166–178.
[16] S. Marié, S. Deck, P. Weiss, From pressure fluctuations to dynamic loads on axisymmetric step flows with minimal number of kulites, Comput. Fluids 39 (5) (2010) 747–755.
[17] S. Marié, H. Lambare, On the unsteady loads induces by the bluff-body wake of the Ariane-5 launcher, in: 6th IUTAM Symposium on the Bluff-Body Wake, Capri, Italy, 2010.
[18] S. Marié, H. Lambaré, P. Druault, A modal overview of the unsteady loads induced by the Ariane 5 base-flow, in: 4th Eur. Conf. for Aerospace Sciences, St-Petersburg, Russia, 2011.
[19] N. Murray, E. Sällström, L. Ukeiley, Properties of subsonic open cavity flow fields, Phys. Fluids 21 (2009) 095103, 16 pp.
[20] M. Ragab, Buffet loads prediction for a launch vehicle and comparison to flight data, J. Spacecr. Rockets 29 (6) (1992) 849–855.
[21] F. Schrijer, A. Sciacchitano, F. Scarano, K. Hannemann, J.-F. Pallegoix, J. Maseland, R. Schwane, Experimental investigation of base flow buffeting on the Ariane 5 launcher using high speed PIV, in: 7th European Symposium on Aerothermodynamics for Space Vehicles, Bruges, Belgium, 2011.
[22] L. Sirovich, Turbulence and the dynamics of coherent structures. Part I: Coherent structures, Q. Appl. Math. XLV (1987) 561–571.
[23] P. Weiss, S. Deck, Zonal Detached Eddy Simulation of the flow dynamics on an Ariane 5-type afterbody, in: 4th Eur. Conf. for Aerospace Sciences, St-Petersburg, Russia, 2011.
[24] P. Weiss, S. Deck, J. Robinet, P. Sagaut, On the dynamics of axisymmetric turbulent separating/reattaching flows, Phys. Fluids 21 (2009) 075103.
[25] H. Wong, J. Meijer, R. Schwane, Experimental and theoretical investigation of base-flow buffeting on Ariane 5 launch vehicles, J. Propuls. Power 23 (1) (2007) 116–122.